Impact of the crystallographic variants of VO2 thin films on c-and r-cut sapphire on structural phase transition and radiofrequency properties

Laura Diebold, Thomas Maroutian, Ludovic Largeau, Nicolas Guiblin, Romain Bude, Guy Garry, Olga M Ishchenko, Pascal Aubert

Impact of the crystallographic variants of VO_2 thin films on c- and r-cut sapphire on structural phase transition and radiofrequency properties

Laura Diebold,[1,2] Thomas Maroutian,[1,a)] Ludovic Largeau,[1] Nicolas Guiblin,[3] Romain Bude,[2] Guy Garry,[2] Olga M. Ishchenko,[2] and Pascal Aubert[1]

[1] *Centre de Nanosciences et de Nanotechnologies (C2N), Université Paris-Saclay, CNRS, Palaiseau, France*
[2] *TE-OX, Orsay, France*
[3] *Laboratoire SPMS, CentraleSupélec, Université Paris-Saclay, CNRS, Gif-sur-Yvette, France*

[a)] Electronic mail: thomas.maroutian@c2n.upsaclay.fr

ABSTRACT

Vanadium dioxide exhibits a metal to insulator transition close to room temperature, making it very interesting in particular for radiofrequency (RF) device applications. Here, we compare the structural and RF properties of VO_2 thin films grown by magnetron sputtering on c-cut and r-cut sapphire substrates. The epitaxial growth of VO_2 on c-cut sapphire gives rise to several crystallographic variants for the insulating M1 phase. Moreover, during the structural transition, simultaneous presence of both metallic and insulating phases is evidenced by X-ray diffraction over a large temperature range. Films grown on r-cut sapphire exhibit only 2 variants, and present a very narrow temperature range of their structural transition. Interestingly, such structural differences of the films grown on c- and r-cut sapphire substrates have very little influence on their dc resistivity, while the transmission of the RF signal through the metallic phase was found much lower on c-cut than on r-cut sapphire. This supports the fact that r-cut sapphire is preferable for VO_2-based RF device fabrication.

Keywords: Vanadium dioxide, X-ray diffraction, Epitaxy, Phase transition, Radiofrequency devices

The growing demand of the Internet of Things pushes the telecommunication industry to find solutions for increasing the data exchange rate and the sustainability of the electronic components. In this picture, phase change materials are appealing to complement classical semiconductors by their ability to adapt their physico-chemical behavior in response to a stimulus. Among these, vanadium dioxide (VO_2) is distinguished from the others by its metal-insulator transition (MIT) at the temperature T_{MIT} around 67°C [1–3]. It exhibits an insulating monoclinic phase VO_2(M1) (space group $P2_1/c$) for $T < T_{MIT}$, and a metallic rutile phase VO_2(R) (space group $P4_2/mnm$) for $T > T_{MIT}$ with a modification of structural, electronic, and optical transmission properties. Additionally, the transition of the VO_2 may be triggered by different stimuli such as thermal [2], mechanical and optical [4,5], directly impacting the transition rate. This makes VO_2 thin films attractive for electronic and optical devices [6] such as radiofrequency (RF) switches, smart windows, and tunable materials with memory effect. In these applications, the transition dynamics of VO_2 play a crucial role, and require high material quality with a steep slope of the electrical resistivity, close to the one obtained for bulk single crystals [3]. The VO_2 thin films growth is already a well-studied topic. The depositions were mainly developed on sapphire (Al_2O_3) substrate [7–10] as high quality VO_2 films were obtained with desired electrical and optical properties. However, due to the lattice parameter and symmetry mismatch between monoclinic VO_2(M1) and hexagonal Al_2O_3 phases, multiple crystallographic variants coexist in the VO_2 film. Crystallographic variants of VO_2 have been known since more than 10 years [11–13], but no report directly address their impact on the phase transition dynamics.

In this work, we aim at exploring the effect of these crystallographic variants on the thermally induced phase transition dynamics of the VO_2(M1/R). The high quality of deposited VO_2 thin films was evidenced by structural characterizations, focusing on the differences between the films grown on two different substrate orientations (c-cut (0001) or r-cut ($1\bar{1}02$) Al_2O_3). While the dc resistivity hysteresis was found very similar on both substrates, we reveal by temperature-dependent X-ray diffraction (XRD) a large temperature region where M1 and R phases coexist for VO_2 deposited on c-cut sapphire, which was not observed for r-cut. We discuss hereafter the impact of these structural differences on the RF properties of the films integrated into devices.

Epitaxial thin films of VO_2, 280 nm-thick as measured by mechanical profilometry after etching, have been grown by RF magnetron sputtering under low oxygen pressure, at the substrate temperature of 525°C, without further post-deposition annealing (see the supplementary material (SM) for more details on the growth). The oxide structure was characterized by Raman spectroscopy and by XRD. The experimental results shown in Fig.1 confirm the monoclinic M1 phase by the three main Raman bands at 192, 223 and 614 cm^{-1} [14,15]. The two first can be associated with the motion of vanadium along the $c_{VO2(M1)}$-axis of the VO_2 crystal (stretching motion of V-V dimers), while the third is related to the stretching mode of V-O vibrations. Structural characterizations performed by XRD and electrical measurements (see Fig.S1 from SM) further underline the excellent crystalline quality of the VO_2 films. The corresponding θ-2θ scans in Fig.1(b) show peaks at 39.81° and 37.07° that can respectively be attributed to $(020)_{VO2(M1)}$ and $(200)_{VO2(M1)}$ planes [16]. Moreover, for each sample, all peaks of the same plane family were indexed. No other diffraction peaks were detected besides the ones of the substrate, which indicates that the obtained VO_2(M1) films on c-cut and r-cut Al_2O_3 are pure phase with the same preferred growth orientation as reported in the state-of-the-art [9,12].

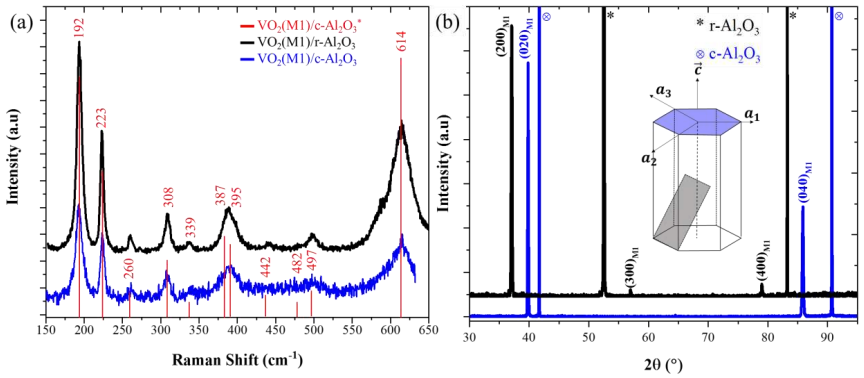

FIG. 1. (a) Raman spectra and (b) θ-2θ scans at room temperature of VO_2 films deposited on c-cut (blue) and r-cut (black) sapphire substrates. The (linear) intensity scale is different for both orientations, with a shift of origin between the two for clarity. The Raman spectra are compared to the one of a 200 nm VO_2 film on (001)Al_2O_3 obtained by electron beam evaporation followed by a post-annealing under oxygen atmosphere (red) [14].

Once the room temperature M1 phase was confirmed, the epitaxial relationships were investigated for the two orientations by φ-scan (Fig.2) and reciprocal space map (RSM, Fig.3) analyses. On c-cut

sapphire (Fig.2(a)), the φ-scan of the oblique plane $(104)_{Al2O3}$ reveals the threefold symmetry of the hexagonal structure of Al_2O_3 along the c_{Al2O3}-axis, visible by the three peaks spaced by 120°, respectively. The φ-scan of $(220)_{VO2(M1)}$ shows six triple peaks spaced by 60°. Combining the intrinsic two-fold symmetry of VO_2 around the $b_{VO2(M1)}$-axis (space group #14 2_1 screw axis) with the threefold symmetry around the c_{Al2O3}-axis gives the pseudo-six-fold symmetry revealed by these six triplets. These same triplets, comprised of one main peak between two smaller satellites spaced by 4.3°, were already reported in several studies [9,12,17,18]. Thanks to XRD scans in high-resolution performed on the satellite and the main peaks (Fig.S2 in SM), we confirmed that the triplets come from two plane families of VO_2(M1), $(220)_{VO2(M1)}$ and $(\bar{2}22)_{VO2(M1)}$. As shown in SM, we detected both at the same time while working in symmetric φ-scan configuration on our setup [12]. Given the two possible orientations of the $c_{VO2(M1)}$-axis, shown in Fig. 2(c), for each of the three $a_{VO2(M1)}$-axis directions, this results into 6 different crystallographic variants for VO_2(M1) phase on c-cut sapphire.

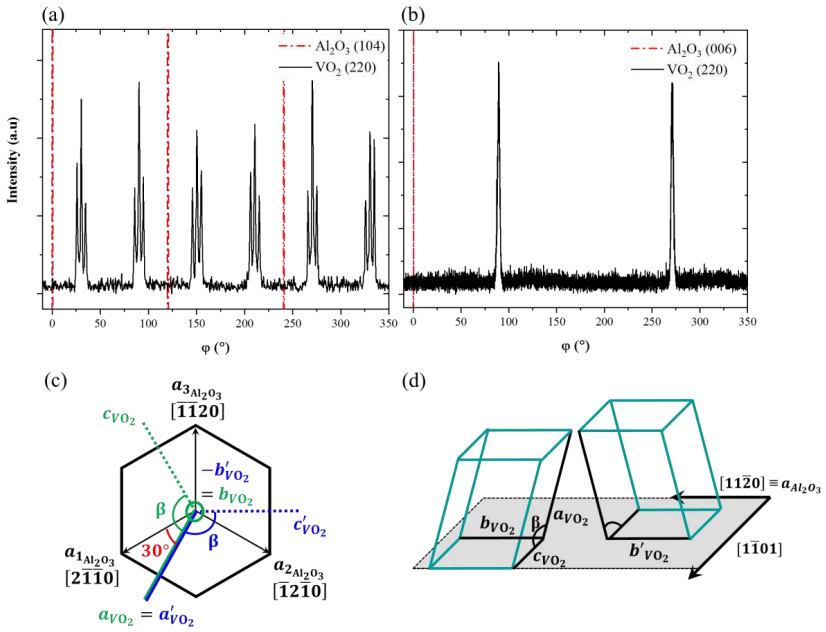

FIG. 2. XRD φ-scans at room temperature of a VO_2 layer deposited on (a) c-cut and (b) r-cut Al_2O_3 substrate. The red dashed lines indicate the positions of the $(104)_{Al2O3}$ and $(006)_{Al2O3}$ planes, respectively. The $(220)_{VO2(M1)}$ scans are shown in black. (c) VO_2(M1) epitaxy on c-cut Al_2O_3 for two variants with their $a_{VO2(M1)}$-axis (green and blue solid lines) at 30° from $a_{1_{Al2O3}}$ azimuth. Their different $c_{VO2(M1)}$-axis orientations (green and blue dotted lines) correspond to $b_{VO2(M1)}$ or its opposite $b'_{VO2(M1)}$ at 180°, respectively. (d) The two variant possibilities of VO_2(M1) deposited on r-cut Al_2O_3 considering a 180° in-plane rotation of $b_{VO2(M1)}$.

By contrast with the case of the c-cut Al_2O_3 substrate, structural studies on VO_2(M1) films deposited on r-cut Al_2O_3 substrate are only scarcely reported in the literature. Here, the φ-scans of the oblique planes

$(006)_{Al2O3}$ and $(220)_{VO2(M1)}$ for a VO_2 film deposited on r-cut sapphire are displayed in Fig.2(b). The results indicate that the trace of $(220)_{VO2(M1)}$ is in the r-cut Al_2O_3 plane, at ±90° of the trace of $(006)_{Al2O3}$ plane. As depicted in Fig.2(d), the $c_{VO2(M1)}$-axis is thus perpendicular to the a_{Al2O3}-axis of Al_2O_3. Since the $b_{VO2(M1)}$ direction is 90° from $c_{VO2(M1)}$, it follows that the $b_{VO2(M1)}$-axis is aligned along the a_{Al2O3}-axis or $[11\bar{2}0]$ direction of the r-plane of Al_2O_3. We note that given VO_2(M1) crystallographic structure, the measured φ-scans on r-cut Al_2O_3 would be the same for a VO_2 variant with its $b_{VO2(M1)}$ unit vector at 180° from the one shown in Fig.2(d). The RSM analyses presented below will evidence that there are indeed two different crystallographic variants for VO_2(M1) phase on r-cut sapphire.

We measured large area RSM in order to confirm the multiple growth variants developed on c- and r-cut Al_2O_3 substrates. Moreover, the different (hkl) plane positions obtained in these RSM allowed us to calculate the film lattice parameters and to determine the strain along the different unit cell axes of VO_2. As the film properties and in particular the MIT dynamics depend on the strain in the VO_2(M1) unit cell, this determination is very important to compare the films between both substrate orientations. Figure 3 displays the RSM obtained for VO_2 films on c- and r-cut Al_2O_3 when aligned with respect to the substrate directions.

In the case of c-cut sapphire, the maps along each of the 3 a_{Al2O3}-axes at φ = 60°, 180°, and 300° were exactly the same, thus only one at φ = 60° is shown in Fig.3(a). In reciprocal space, the Q_y direction is aligned with one a_{Al2O3}-axis, while the Q_z direction is along the c_{Al2O3}-axis. All the diffraction peaks can be identified, belonging either to the substrate (yellow circles and grid) or to two different VO_2 variants (red and grey circles, respectively). Besides the $(020)_{VO2(M1)}$ and $(040)_{VO2(M1)}$ spots observed at $Q_y = 0$ (red and grey double circles), in agreement with the θ-2θ scan of Fig.1(b), diffraction spots from both the $(\bar{h}kh)_{VO2(M1)}$ and $(0kl)_{VO2(M1)}$ families are detected on the RSM. As depicted on the left of Fig.3(a) in the case of $(\bar{1}11)$ and (011) planes, these planes cannot belong to the same variant but are from two variants with their a_{VO2M1}-axes 60° apart. Together with the data from the identical RSM measured at φ = 120° and 300°, 3 different crystallographic variants are detected for VO_2(M1). The resolution on the φ angle is not enough to discriminate in the RSM between the variants with their $b_{VO2(M1)}$-axis parallel or anti-parallel to the c_{Al2O3}-axis, but they are clearly identified through the φ-scan of $(220)_{VO2(M1)}$ (Fig.2(a) and (c)). In this way, we confirm the 6 different orientations of the VO_2(M1) unit cell on c-cut sapphire.

On r-cut sapphire, the RSM taken in opposite directions at φ = 0° and 180° are different, as shown in Fig.3 (b) and (c), respectively. This evidences the presence of 2 crystallographic variants, with opposite in-plane directions of their $b_{VO2(M1)}$-axes as depicted in Fig.2(d) and reproduced on the left of Fig.3(b) and (c). Indeed, as the $a_{VO2(M1)}$-axis is positioned out-of-plane at an angle β~122° (Table S1 in SM) from $c_{VO2(M1)}$, a RSM along the φ = 0° or 180° azimuth is parallel to the $c_{VO2(M1)}$-axis and thus is sensitive to the direction of the $a_{VO2(M1)}$-axis with respect to the surface plane. As shown in Fig.3(b) and (c), for example the (-102), (-202), (202) and (002) planes are all seen on the RSM but ascribed to two different variants, with spot intensities depending on the φ = 0° or 180° direction of the RSM. While one variant will show the (-102) and (-202) spots at φ = 0° (Fig. 3(b), in grey), it will exhibit the (202) and (002) spots at φ = 180° (Fig.3(c), in grey). And the opposite is observed for the other variant (in red in Fig.3(b) and (c)). Finally, 2 crystallographic variants of VO_2(M1) are detected on r-cut sapphire.

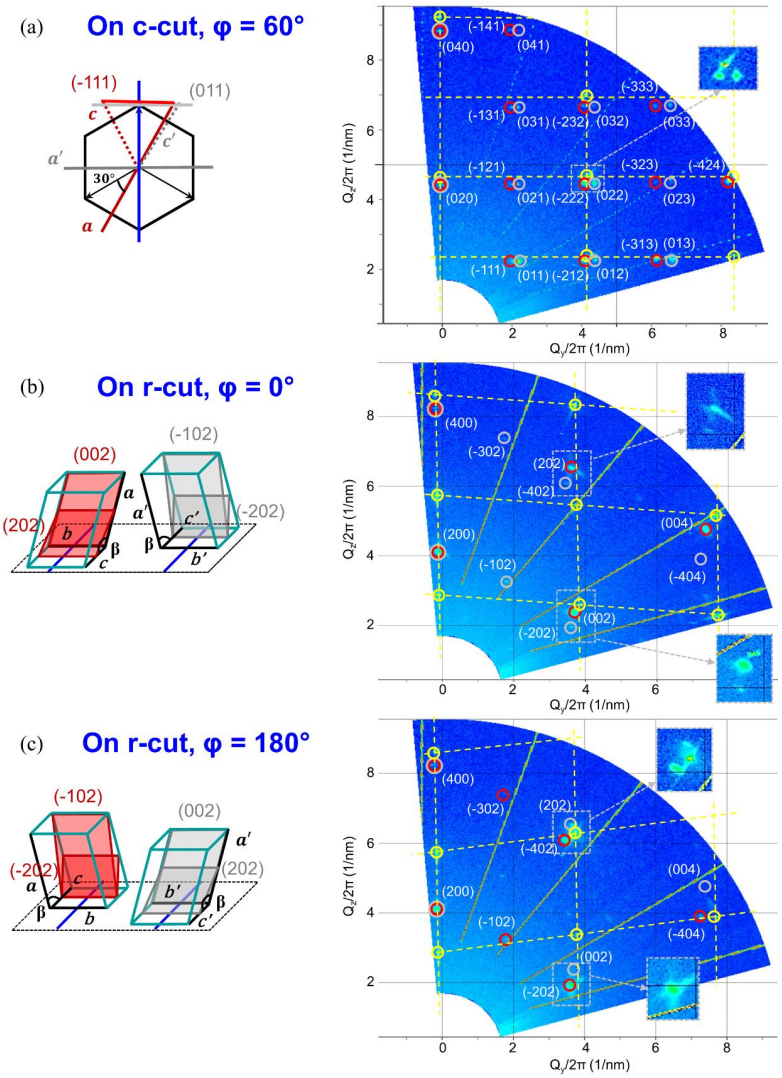

FIG. 3. Reciprocal space maps (RSM) of VO_2(M1) deposited on (a) c-cut sapphire substrate, taken along a_{Al2O3} azimuth, and (b, c) on r-cut sapphire, taken perpendicular to a_{Al2O3} azimuth with (b) along $[1\bar{1}01]$ and (c) along $[\bar{1}101]$. The directions of the RSM scans are shown as blue lines on the unit cell sketches on the left of each map. The substrate peaks and reciprocal space lattice are shown in yellow. The VO_2(M1) peaks are indexed in white and circled in red or grey to differentiate between the two variants seen on each map. These variants are depicted on the left in corresponding colors (red and grey), with a few selected planes as example, to be related to the peaks seen on the maps. Close-up views of some areas of the RSM are also shown, to underline the 2 VO_2(M1) variants detected on each map.

From the indexed diffraction spot positions on the RSM, we were able to calculate the lattice parameters of the VO_2(M1) films on c- and r-cut sapphire. The results are presented in the SM (Table S1), with strain values lower than 1% on all three a, b and c axes of the unit cell for both substrate orientations. This indicate mostly relaxed films, and is also compatible with the domain matching epitaxy (DME) mechanism proposed by Narayan *et al*. [19,20] We measured a slightly lower compressive strain along the $a_{VO2(M1)}$-axis on c-cut (-0.4%) than on r-cut (-0.7%) sapphire (Table S1). This is not enough of a difference to give a significant shift of the MIT temperature [21, 24] between the two substrates.

As not only strain but also VO_2 film microstructure can strongly impact materials property [20], we sought whether multiple variants induce modifications in the transition dynamics, the property that makes VO_2 attractive. Therefore, the structural transition of VO_2 was investigated by temperature assisted XRD measurements (Fig.4). The θ-2θ scans were acquired in the temperature range between 27°C to 92°C for VO_2(M1) films, and the $(020)_{VO2(M1)}$ and $(200)_{VO2(M1)}$ peak parameters were determined by a fit with pseudo-Voigt functions. Fig.4 (a) and (b) show the evolution of the VO_2 peak position as function of temperature on c- and r-cut sapphire substrates, respectively.

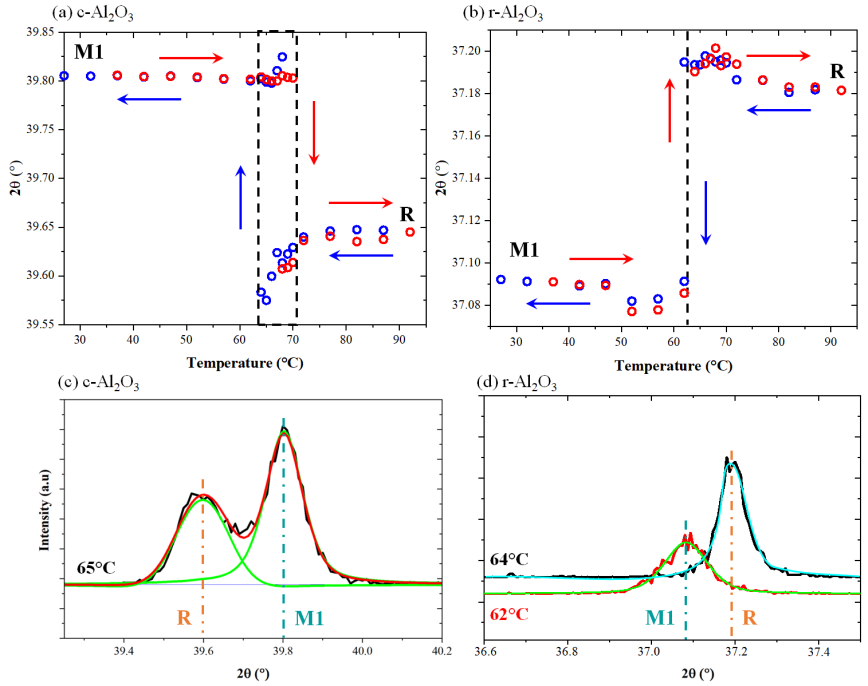

FIG. 4. Evolution of the VO_2(M1) peak positions as function of temperature (heating in red and cooling in blue, vertical dotted lines are guide to the eye) on (a) c-cut and (b) r-cut Al_2O_3. Selected θ-2θ scans at (c) 65°C and (d) between 62°C and 64°C are shown to evidence the phase coexistence on c-cut sapphire (c), not seen on r-cut sapphire (d). Experimental data in black and fit in green, red and blue, with peak positions indicated by vertical dash-dotted lines.

For the film deposited on c-cut Al_2O_3 (Fig.4(a)), three distinct zones can be observed. Between ambient temperature and 60°C, the position of the $(020)_{VO2(M1)}$ peak remains stable. Starting from 62°C, the peak position shifts slightly towards higher 2θ values. This phenomenon is accentuated when a second diffraction peak appears, corresponding to the R phase. Between 64°C and 70°C, there is coexistence of these two peaks. Considering the multiple crystallographic variants of VO_2 on c-cut Al_2O_3 and the resulting polycrystalline microstructure (see also topography images in SM, Fig.S3), the phase transition can happen step by step. When thermal stimulus is applied, crystallites of the insulating phase will transit to the metallic phase. As the temperature increases, the R phase proportion will increase. And since the metallic R phase has higher density than the M1 phase, local strain on the crystallites can appear and explain the slight 2θ shift of the peak. Finally, when the temperature is higher than 75°C, the second peak stabilizes around $2\theta = 39.64°$, corresponding to the (020) plane of the rutile phase. The same phenomenon was observed upon cooling, and a phase coexistence region is clearly evidenced (Fig.4(c)). In the case of the film on r-cut Al_2O_3, the evolution of the VO_2 diffraction peak in the 36.5° to 37.5° 2θ range (Fig.4(b)) also confirms the phase transition but without phase coexistence for the M1 and R phases. While some earlier works reported an intermediate M2 phase during the temperature-induced transition [21,23], all the films grown in our study by RF magnetron sputtering transit directly from M1 to R or with a coexistence of M1 and R phases alone. It is likely that local strain developed during VO_2 growth along $a_{VO2(M1)}$-axis (or $c_{VO2(R)}$) impact the formation of the new phase [22–24]. In particular, under compressive strain the film will tend to transit directly from M1 to R, as observed here.

At variance with the dc resistivity properties, for which experimental results are similar on both substrate orientations (Fig.S1 in SM), with hysteresis widths <1°C and resistivity ratio of 10^4, structural transition results (Fig.4) evidence the high impact of the crystallographic variants on VO_2 transition dynamics. Following this observation, and in order to assess the possible effect on performance for RF applications, we fabricated RF switches, using classical fabrication processes [25] , comprised of a patch of active VO_2 material integrated with gold coplanar waveguides as shown in Fig.5(a). The exact same process was used to develop VO_2-RF switches in so-called series configuration on both orientations of the Al_2O_3 substrate. After checking that VO_2 patterns were not affected by the process, and in particular that the crystalline quality was not altered (Fig.S4 in SM), RF characterizations were performed as a function of temperature. Fig.5(b) is an example of results obtained for switches fabricated on c- and r-cut sapphire. In both cases, our measurements show that VO_2 switches in series configuration present the same general behavior indifferently of the substrate orientation used. The signal is reflected when the VO_2 is insulating, and transmitted when the VO_2 is in the metallic state. However, it should be noted that in the case of switches fabricated on c-cut Al_2O_3, from the mean values reported in Table 1, the insertion losses were higher (3.3±0.7 dB at 10 GHz) that on r-cut (1.2±0.3 dB at 10 GHz). Incidentally, this is in line with the slightly higher resistivity measured at 80°C for VO_2(R) phase on c-cut sapphire compared to r-cut (Fig.S1 in SM). There thus appears to be a link between polycrystalline microstructure and resistivity in the metallic phase. According to the percolation theory [26], the metallic phase resistivity depends on the formation and percolation of conductive clusters, influenced by the local mechanical stresses. In this picture, the crystallographic variants would affect the formation of a conductive path between the crystallites, giving a higher resistivity for a higher number of different orientations of the crystallites, as is the case for VO_2(R) on c-cut compared to r-cut sapphire. This in turn results in a lower transmission of the RF signal for the metallic phase on c-cut than on r-cut at RF frequencies.

Table 1. Comparison of VO_2 switch performance in series configuration for VO_2 deposited on c-cut and r-cut Al_2O_3 substrates. Both mean values and standard deviations (Std dev) are given, in red for metallic state (at 80°C) and in blue for the insulating one (at room temperature).

VO_2 switch series configuration	**Insertion loss (dB) at 10 GHz**		**Isolation (dB) at 10 GHz**	
	Mean value	Std dev	Mean value	Std dev
r-cut Al_2O_3	1.2	0.3	31.2	0.8
c-cut Al_2O_3	3.3	0.7	31.3	2.6

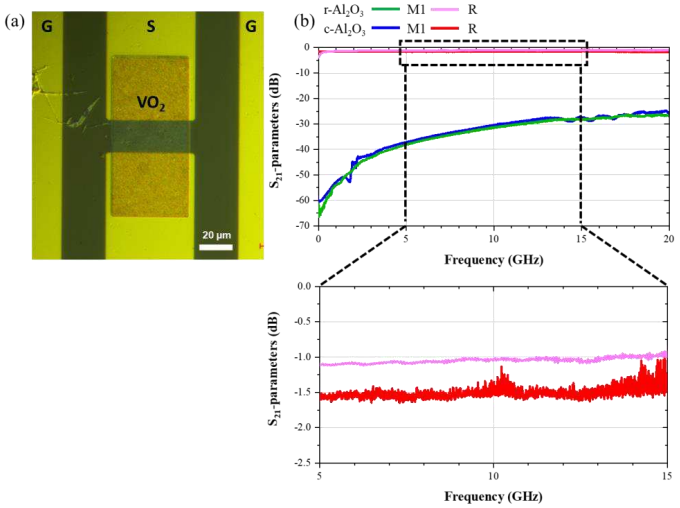

FIG. 5. (a) Optical micrograph of fabricated RF switches in series configuration. (b) S_{21}-parameters measured at room temperature (M1 phase) and at 80°C (R phase). The VO_2 thin film was deposited on r-cut Al_2O_3 (in green and pink) and c-cut Al_2O_3 (in blue and red).

In conclusion, our investigations on VO_2(M1) films grown by RF magnetron sputtering on c- and r-cut sapphire substrates demonstrated the key role of the substrate orientation. Different preferential growth orientations are obtained, $(0k0)_{VO2(M1)}$ on c-cut Al_2O_3 with 6 possible crystallographic variants, and $(h00)_{VO2(M1)}$ on r-cut Al_2O_3 with only 2 variants. Despite the temperature-dependent dc resistivity measurements show very close dynamics for both samples, clear differences arise looking at the structural transition and at the conduction properties in the RF range. Considering this, we can affirm that the growth mode induced by the two substrate orientations impacts the transition dynamics, with a final outcome on device performance in the RF range. The evidence of coexisting insulator and metallic states of VO_2 during the transition for films deposited on c-cut Al_2O_3 substrate could certainly explain the lower performances of switches for this orientation. This calls for additional studies of frequency-dependent resistivity measurements as a function of VO_2 grain size and grain boundary structure.

SUPPLEMENTARY MATERIAL

See the supplementary material for details about thin film growth, resistivity hysteresis measurements during VO_2 phase transition, additional X-ray diffraction data including lattice parameter calculations, thin film morphology, and RF switches fabrication.

ACKNOWLEDGEMENTS

The authors would like to thank L. Floyd and M. Modreanu (Tyndall National Institute, Ireland) for their help with the RF measurements. We are also grateful to C. Brochard, J. Chaste and A. Ouerghi (C2N) for the Raman measurements and helpful discussions. We acknowledge the ANRT for financial support, grant N°2018/1494, and the Direction Générale de l'Armement under agreement N°192906070 in the framework of the RAPID program. This project has received funding from the European Union Horizon 2020 Research and Innovation Program in the frame of Nano-EH, FETPROACT-EIC project, grant agreement N°951761. Research at the Centre for Nanoscience and Nanotechnology was partly supported by the French RENATECH network.

DATA AVAILABILITY

The data that supports the findings of this study are available within the article and its supplementary material.

REFERENCES

[1] J.B. Goodenough, "The two components of the crystallographic transition in VO_2," J Solid State Chem **3**(4), 490–500 (1971).

[2] F.J. Morin, "Oxides which show a metal-to-insulator transition at the Neel temperature," Phys Rev Lett **3**(1), 34–36 (1959).

[3] J. Duchene, M. Terraillon, and M. Pailly, "R.F. and D.C. reactive sputtering for crystalline and amorphous VO_2 thin film deposition," Thin Solid Films **12**(2), 231–234 (1972).

[4] T.L. Cocker, L. v. Titova, S. Fourmaux, G. Holloway, H.C. Bandulet, D. Brassard, J.C. Kieffer, M.A. el Khakani, and F.A. Hegmann, "Phase diagram of the ultrafast photoinduced insulator-metal transition in vanadium dioxide," Phys Rev B Condens Matter Mater Phys **85**(15), 1–11 (2012).

[5] D. Wegkamp, and J. Stähler, "Ultrafast dynamics during the photoinduced phase transition in VO2," Prog Surf Sci **90**(4), 464–502 (2015).

[6] Y. Ke, S. Wang, G. Liu, M. Li, T.J. White, and Y. Long, "Vanadium Dioxide: The Multistimuli Responsive Material and Its Applications," Small **14**(39), 1–29 (2018).

[7] E.N. Fuls, D.H. Hensler, and A.R. Ross, "Reactively sputtered vanadium dioxide thin films," Appl Phys Lett **10**(7), 199–201 (1967).

[8] G. Garry, O. Durand, and A. Lordereau, "Structural, electrical and optical properties of pulsed laser deposited VO_2 thin films on R- and C-sapphire planes," Thin Solid Films **453–454**, 427–430 (2004).

[9] Y. Zhao, J. Hwan Lee, Y. Zhu, M. Nazari, C. Chen, H. Wang, A. Bernussi, M. Holtz, and Z. Fan, "Structural, electrical, and terahertz transmission properties of VO_2 thin films grown on c-, r-, and m-plane sapphire substrates," J Appl Phys **111**(5), (2012).

[10] V. Théry, A. Boulle, A. Crunteanu, J.C. Orlianges, A. Beaumont, R. Mayet, A. Mennai, F. Cosset, A. Bessaudou, and M. Fabert, "Structural and electrical properties of large area epitaxial VO_2 films grown by electron beam evaporation," J Appl Phys **121**(5), (2017).

[11] F.J. Wong, Y. Zhou, and S. Ramanathan, "Epitaxial variants of VO_2 thin films on complex oxide single crystal substrates with 3m surface symmetry," J Cryst Growth **364**, 74–80 (2013).

[12] L.L. Fan, Y.F. Wu, C. Si, G.Q. Pan, C.W. Zou, and Z.Y. Wu, "Synchrotron radiation study of VO_2 crystal film epitaxial growth on sapphire substrate with intrinsic multi-domains," Appl Phys Lett **102**(1), (2013).

[13] L.L. Fan, Y.F. Wu, C. Si, C.W. Zou, Z.M. Qi, L.B. Li, G.Q. Pan, and Z.Y. Wu, "Oxygen pressure dependent VO_2 crystal film preparation and the interfacial epitaxial growth study," Thin Solid Films **520**(19), 6124–6129 (2012).

[14] F. Ureña-Begara, A. Crunteanu, and J.P. Raskin, "Raman and XPS characterization of vanadium oxide thin films with temperature," Appl Surf Sci **403**, 717–727 (2017).

[15] P. Shvets, O. Dikaya, K. Maksimova, and A. Goikhman, "A review of Raman spectroscopy of vanadium oxides," Journal of Raman Spectroscopy **50**(8), 1226–1244 (2019).

[16] Joint Committee on Powder Diffraction Standards (JCPDS) file #01-082-0661.

[17] B. Hong, K. Hu, Z. Tao, J. Zhao, N. Pan, X. Wang, M. Lu, Y. Yang, Z. Luo, and C. Gao, "Polymorph separation induced by angle distortion and electron delocalization effect via orbital modification in VO_2 epitaxial thin films," Phys Rev B **95**(7), 1–8 (2017).

[18] C. Chen, Y. Zhu, Y. Zhao, J.H. Lee, H. Wang, A. Bernussi, M. Holtz, and Z. Fan, "VO_2 multidomain heteroepitaxial growth and terahertz transmission modulation," Appl Phys Lett **97**(21), 3–6 (2010).

[19] J. Narayan, and B.C. Larson, "Domain epitaxy: A unified paradigm for thin film growth," J Appl Phys **93**(1), 278–285 (2003).

[20] J. Narayan, and V.M. Bhosle, "Phase transition and critical issues in structure-property correlations of vanadium oxide," J Appl Phys **100**(10), (2006).

[21] V. Théry, A. Boulle, A. Crunteanu, J.C. Orlianges, A. Beaumont, R. Mayet, A. Mennai, F. Cosset, A. Bessaudou, and M. Fabert, "Role of thermal strain in the metal-insulator and structural phase transition of epitaxial VO_2 films," Phys Rev B **93**(18), 1–9 (2016).

[22] J.P. Pouget, H. Launois, J.P. D'Haenens, P. Merenda, and T.M. Rice, "Electron Localization Induced by Uniaxial Stress in Pure VO2," Phys Rev Lett **35**(13), 873–875 (1975).

[23] L. Rodríguez, F. Sandiumenge, C. Frontera, J.M. Caicedo, J. Padilla, G. Catalán, and J. Santiso, "Strong strain gradients and phase coexistence at the metal-insulator transition in VO2 epitaxial films," Acta Mater **220**, (2021).

[24] H. Guo, K. Chen, Y. Oh, K. Wang, C. Dejoie, S.A. Syed Asif, O.L. Warren, Z.W. Shan, J. Wu, and A.M. Minor, "Mechanics and dynamics of the strain-induced M1-M2 structural phase transition in individual VO2 nanowires," Nano Lett **11**(8), 3207–3213 (2011).

[25] O.M. Ishchenko, F. Hamouda, P. Aubert, O. Tandia, M. Modreanu, D.I. Sharovarov, F.Y. Akbar, A.R. Kaul, and G. Garry, "Strongly Electronic-Correlated Material for Ultrafast Electronics Application," Proceedings of the IEEE Conference on Nanotechnology **2018-July**, 420–425 (2019).

[26] C. Koughia, O. Gunes, C. Zhang, S.-J. Wen, R. Wong, Q. Yang, and S. O. Kasap, "Topology of conductive clusters in sputtered high-quality VO2 thin films on the brink of percolation threshold during insulator-to-metal and metal-to-insulator transition," Journal of Vacuum Science & Technology A **38**(6), 063401 (2020).